Supplementary Material: Future Projections and Uncertainty Assessment of Precipitation Extremes in Iran from the CMIP6 Ensemble

Juyoung Hong [1], Khadijeh Javan [2], Yonggwan Shin [1], and Jeong-Soo Park [1,*]

1: Department of Mathematics and Statistics, Chonnam National University, Gwangju 61186, Korea.

2: Department of Geography, Urmia University, Urmia 009844, Iran.

**: Corresponding author, E-mail: jspark@jnu.ac.kr, Tel: +82-62-530-3445*

August 16, 2021

1 Data and simulation models

Table S1 lists 24 climate models used in this study. Figure S2 shows examples of time series plots of the observations (blue line) and the bias-corrected data of a simulation model, for the AMP1 (Annual Maximum Daily Precipitation). Green lines represent no-bias-corrected historical data whereas red lines represent the bias-corrected data in each grid point (G10, G17, G24, and G42).

2 Multivariate bias correction

When bias-correction (BC) such as quantile mapping is used, most model weights based on performance become equal because of a perfect matching [1], and thus, the prediction is same as the simple average of the bias-corrected model outputs. This is approximately true for the MBC (Multivariate Bias Correction) [2] employed in this study because the MBC is a multivariate generalization of quantile mapping. Thus, the historical data is not bias corrected. No-bias-corrected historical data are utilized to calculate the performance weight of a model.

Chen et al.[3] found that the bivariate BC of rainfall and air temperature led to a much better performance than univariate BC. Cannon [2] proposes a multivariate generalization of quantile mapping (QM). It is an iterative method which conceptually lays between univariate bias correction (BC) methods and the empirical copula-based correction (EC-BC) [4]. For a

univariate BC, the quantile delta mapping (QDM) [5] is used, which preserves trends of model data

It approximately preserves the multivariate dependence of the driving climate model. Here, an image processing technique—the N-dimensional probability density function transform (N-pdft)—designed to transfer color information from one image to another is adapted. In each iteration, univariate QM is first applied separately to each variable. Then a multivariate BC is employed by re-scaling the multivariate anomalies based on Cholesky decomposition of the covariance matrix. The algorithm ends when both the corrected marginals and the dependence structure are sufficiently close to their observed counter parts. A variant is based on ranks rather than on the actual values [1]. It provides a multivariate quantile delta mapping, referred to as MBCn (multivariate bias correction with N-pdft) algorithm. It consists, in each iteration, of a random orthogonal rotation of multivariate input data, a univariate quantile delta mapping on the rotated fields and the inverse rotation. This algorithm approximately preserves trends of model data. We used the 'MBC' package [6] in R for computation. More details are found in Cannon [2].

3 Computing weights

3.1 Performance weights

To compute the performance of each model, T-year return levels are compared based on the GEVD(Generalized Extreme Value Distribution) fitting on the historical data and the observations. Let us denote r_T^i and r_T^0 as T-year return level obtained from the historical data of i-th model and the observations, respectively. These values are normalized as follows to make it scale-free, for $i = 0, 1, \cdots, M$:

$$\tilde{r}_T^i = \frac{r_T^i - med_i}{R_i}, \tag{1}$$

where

$$R_i = \begin{cases} max_i - med_i & \text{if } r_T^i \geq med_i, \\ med_i - min_i & \text{if } r_T^i < med_i, \end{cases} \tag{2}$$

and max_i, min_i, and med_i are the maximum, the minimum, and the median of i-th model data. Other ways of standardizations are also possible.

The distance for performance measure is calculated by

$$D_i^2 = \sum_T (\tilde{r}_T^i - \tilde{r}_T^0)^2. \tag{3}$$

We set $T = 2$, 5, 10, 20, 30, 50, and 100. Note that D_i does not depend on the shape parameter σ_D, and so obtained D_is are fixed for the next computation.

3.2 Independence weights

To calculate the model similarity S_{ij}, we follow a technique among several methods proposed by Sanderson et al. [7]. A method employed in this study is based on the empirical orthogonal function (EOF) or principal component analysis. The following process is done for each grid: First, for each model, the historical data and the future simulation data from three scenarios are lined up as one time series data. The bias correction is not applied to all data for this process. We can choose the historical data only, as was done by Brunner et al. [8], but we deploy all simulation data for a maximum use of available information. For each time series induced from each model, seven year moving averages are obtained. Then, a correlation matrix R among all M models is constructed by applying the Spearman correlation coefficients to those M numbers of the series of seven year moving averages, for each climate variable. That is, R is the correlation matrix of M models, with size $M \times M$.

A singular value decomposition (SVD) is applied to $R^{1/2}$ and truncated to t modes to calculate the dominant modes of multivariate ensemble variability such that

$$R^{1/2} = U\lambda V^T, \tag{4}$$

where U is an orthogonal matrix of model loadings (M by t size) whose columns are the eigenvectors of the model correlation matrix R, λ (t by t) are the eigenvalues of R, and V (M by t) are the eigenvectors of R. The dimensions are sorted by decreasing eigenvalue, such that the basis set can be truncated to a smaller number of modes t [7]. Note that t is often determined by selecting a number of the eigenvalues greater than 1.

The model loadings U define a t-dimensional space in which intermodel and observation–model Euclidean distances may be defined, where t is the truncation length of the SVD. The inter-model distances are measured in a Euclidean sense in the loadings matrix, so that the distances S_{ij} between two models i and j are expressed as [7]

$$S_{ij} = \left\{ \sum_{l=1}^{t} [U(i,\, l) - U(j,\, l)]^2 \right\}^{1/2}. \tag{5}$$

$U(i,\, l)$ is interpreted as a correlation or a dependency of the model i to the l-th principal component. Thus, a small S_{ij} value means high dependency or similarity between models i and j.

The above procedures are done separately for each of five climate variables. Thus, we have five distances between models i and j, corresponding to five climate variables. Then, the final distances are computed by averaging those five distances for models i and j.

3.3 Selection of σ_S

To select an appropriate value of the shape parameter σ_S for the I-weights, we follow an entropy-based approach by Shin et al.[9]. We denote $I_i(\sigma_S)$ as a normalized I-weight for model i and for the given σ_S, as defined in the following:

$$I_i(\sigma_S) \;=\; \frac{s_i(\sigma_S)}{\sum_{l=1}^{M} s_i(\sigma_S)}, \tag{6}$$

where $s_i(\sigma_S) = \frac{1}{1+\sum_{j\neq i}^{M} exp(-\frac{S_{ij}}{\sigma_S})}$.

The entropy of the I-weights as a measure of uncertainty [10] from these weights is defined by the following:

$$E(\sigma_S) \;=\; -\sum_{i=1}^{M} I_i(\sigma_S) \log I_i(\sigma_S) \tag{7}$$

as a function of σ_S. When all $I_i(\sigma_S)$s are almost equal, the entropy has a high value. We thus expect the entropy to increase because σ_S has a large value. Note that the calculation of S_{ij} does not depend on σ_S, and thus, the S_{ij} values obtained are fixed for the entropy computation. The entropy is computed as σ_S changes from 0.1 to 1.0 in increments of 0.01.

Figure 1 presents the entropy function of σ_S computed from the data used for this study, which indicates that it is at its minimum at $\sigma_S = 0.4$. It is interesting to note that the entropy function increases as σ_S decreases from 0.4 to zero. This is explained by looking into the similarity measure $1 + \sum_{j\neq i}^{M} exp(-\frac{S_{ij}}{\sigma_S})$. As σ_S moves toward zero, this measure converges at one for all i. Thus, s_i moves toward one, and I_i is close to $1/M$ for all i. Because we want to have a shape parameter σ_S that can differentiate the I-weights most distinctly with minimum uncertainty, the value $\sigma_S = 0.4$ minimizing the entropy is chosen in this study.

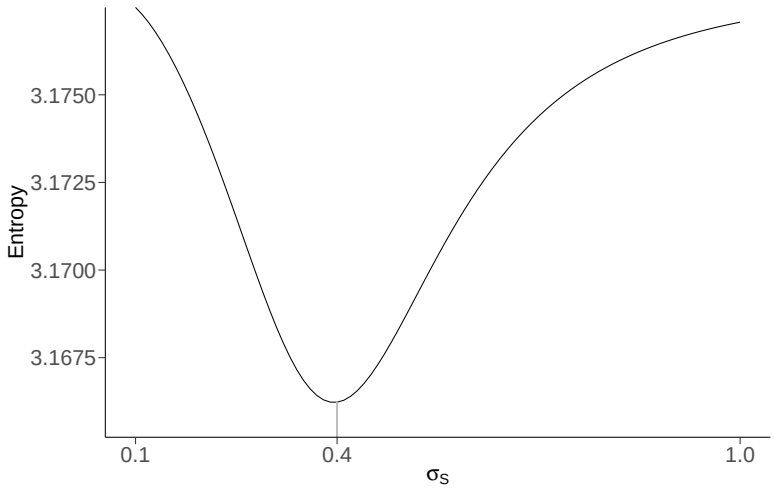

Figure S 1: Plot of the entropy as σ_S changes from 0.1 to 1.0 and the selected $\sigma_S = 0.4$.

4 Result

4.1 Relative change

The relative change of 20 year return level in the period P1 relative to the reference period P0 is defined as:

$$\delta R_{20}(P1) = \frac{R_{20}(P1) - R_{20}(P0)}{R_{20}(P0)} \times 100, \tag{8}$$

where $R_{20}(P)$ is the 20 year return level in the period P.

4.2 Return period and exceedance probability

We have experienced some technical flaws in computing the waiting time or the return periods corresponding to a return value. For example, the resulting return period sometimes turns out to be greater than 500 years even though it is expected to correspond to 50 years. It may be due to the cumulation of truncation or rounding errors in computer, related to inverting the quantile function of the GEVD. A trouble caused by this flow does not vanish even applied to unequally weighted regional frequency analysis (RFA). In this study, we thus adopted the trimmed mean [11] in RFA in which unfairly high estimates of return periods are deleted in computing the weighted average. The defects of return periods are described in Serinaldi [12].

The spatially averaged estimates of exceedance probability over Iran are presented in Figure S5 and in Table S5.

References

[1] Maraun D, Widmann M (2018) *Statistical downscaling and bias correction for climate research.* Cambridge Univ Press.

[2] Cannon AJ (2018) Multivariate quantile mapping bias correction: an N-dimensional probability density function transform for climate model simulations of multiple variables. Clim Dyn 50:31–49.

[3] Chen J, Li C, Brissette FP, Chen H, Wang M, Essou GRC (2018) Impacts of correcting the inter-variable correlation of climate model ouputs on hydrological modeling. J Hydrol 560:326–341.

[4] Vrac M, Friederichs P (2015) Multivariate-intervariable, spatial, and temporal-bias correction. J Clim 28:218–237.

[5] Cannon AJ, Sobie SR, Murdock TQ (2015) Bias correction of GCM precipitation by quantile mapping: How well do methods preserve changes in quantiles and extremes? J Climate 28:6938–6959.

[6] Cannon AJ (2018) Package 'MBC' in R, version 0.10-4. https://cran.r-project.org/web/packages/MBC/MBC.pdf

[7] Sanderson, B.M.; Knutti, R.; Caldwell, P. Addressing interdependency in a multimodel ensemble by interpolation of model properties. *J. Clim.* **2015**, *28*, 5150–5170.

[8] Brunner, L.; Pendergrass, A.G.; Lehner, F.; Merrifield, A.L.; Lorenz, R.; Knutti, R. Reduced global warming from CMIP6 projections when weighting models by performance and independence. *Earth Syst. Dyn. Discuss.* **2020**, *11*, 995–1012, doi:10.5194/esd-2020-23.

[9] Shin, Y.; Shin, Y.; Hong, J.; Kim, M.-K.; Byun, Y.-H.; Boo, K.-O.; Chung, I.-U.; Park, D.-S.R.; Park, J.-S. Future Projections and Uncertainty Assessment of Precipitation Extremes in the Korean Peninsula from the CMIP6 Ensemble with a Statistical Framework. *Atmosphere* **2021**, *12(1)*, 97.

[10] Ross, S. *A First Course in Probability*, 8th ed.; Pearson Prentice Hall: Upper Saddle River, NJ, USA, 2010.

[11] Wilks D (2011) *Statistical Methods in the Atmospheric Sciences,* 3rd Ed., Academic Press, New York.

[12] Serinaldi F (2015) Dismissing return periods! Stoch Environ Res Risk Assess 29:1179–1189. https://doi.org/10.1007/s00477-014-0916-1

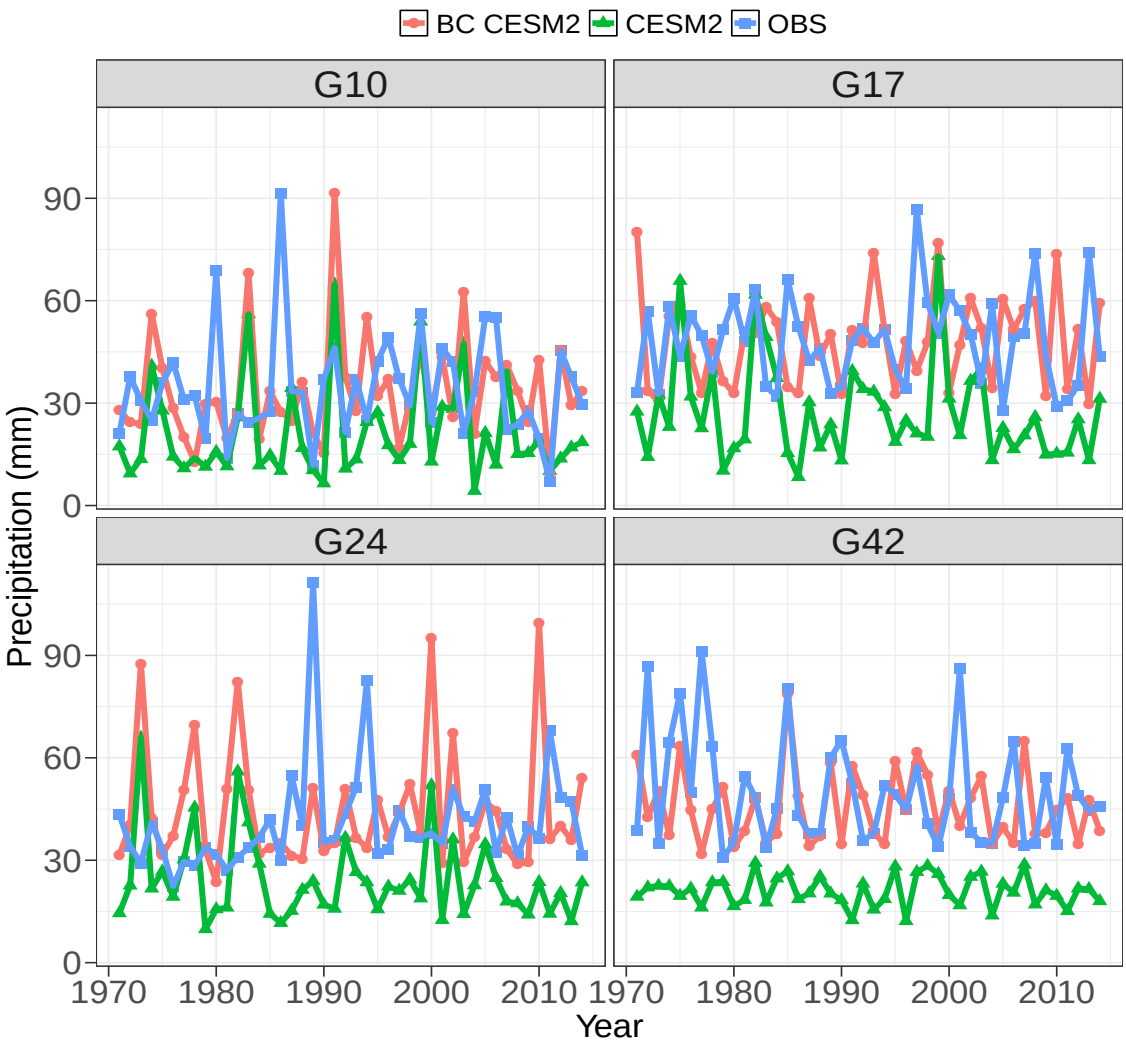

Figure S 2: Examples of time series plots to show the bias correction of the CESM2 simulation data (green line) to the observations (blue line), where red lines represent the bias-corrected data in each grid point (G10, G17, G24, and G42).

Table S 1: The list of 24 CMIP6 (Coupled Model Intercomparison Project Phase 6) models analyzed in this study. The detaied information on each model are available at ESGF-node https://esgf-node.llnl.gov/projects/cmip6/.

Model Name	Institution	Country	Resolution (Lon × Lat Level)
ACCESS-CM2	CSIRO, ARCCSS (Australian Res Council Centre of Excellence for Clim System Sci)	Australia	192×144 L85
ACCESS-ESM1-5	Commonwealth Scientific & Industrial Res Organ (CSIRO)	Australia	192×145 L38
BCC-CSM2-MR	Beijing Clim Center	China	320×160 L46(T106)
CanESM5	Canadian Centre Clim Model & Analysis, Enviro & Clim Change (CCCma)	Canada	128×64 L49(T63)
CESM2-WACCM	Nat Center for Atmos Res, Clim & Global Dynamics Lab (NCAR)	USA	288×192 L70
CESM2	Nat Center for Atmos Res, Clim & Global Dynamics Lab (NCAR)	USA	288×192 L32
CMCC-CM2-SR5	Fondazione Centro Euro-Mediterraneo sui Cambiamenti Climatici(CMCC)	Italy	288×192 L30
CMCC-ESM2	Fondazione Centro Euro-Mediterraneo sui Cambiamenti Climatici(CMCC)	Italy	288×192 L30
EC-Earth3-Veg-LR	EC-Earth consortium, Swedish Meteo & Hydro Inst/SMHI, Sweden	EU	320×160 L62(TL255)
EC-Earth3-Veg	EC-Earth consortium, Swedish Meteo & Hydro Inst/SMHI, Sweden	EU	512×256 L91(TL255)
EC Earth 3.3	EC-Earth consortium, Swedish Meteo & Hydro Inst/SMHI, Sweden	EU	512×256 L91(TL255)
FGOALS-g3	Chinese Academy of Sciences (CAS)	China	180×80 L26
GFDL-ESM4	National Oceanic & Atmos Admi, Geophy Fluid Dynamics Lab	USA	360×180 L49
INM-CM4-8	Inst for Numerical Math, Russian Acad of Sci (INM)	Russia	180×120 L21
INM-CM5-0	Inst for Numerical Math, Russian Acad of Sci (INM)	Russia	180×120 L73
IPSL-CM6A-LR	Institut Pierre Simon Laplace (IPSL)	France	144×143 L79
KACE1.0-GLOMAP	National Inst of Meteo Sci/Meteo Admin, Clim Res Div (NIMS-KMA)	Korea	192×144 L85
MIROC6	JAMSTEC, AORI, NIES, R-CCS (MIROC)	Japan	256×128 L81(T85)
MPI-ESM1.2-HR	Max Planck Inst for Meteo (MPI-M)	Germany	384×192 L95(T127)
MPI-ESM1.2-LR	Max Planck Inst for Meteo (MPI-M)	Germany	192×96 L47(T63)
MRI-ESM2.0	Meteoro Research Institute (MRI)	Japan	320×160 L80(TL159)
NorESM2-LM	NorESM Consortium of CICERO, MET-Norway, NERSC, NILU, UiB, UiO, UNI	Norway	144×96 L32
NorESM2-MM	NorESM Consortium of CICERO, MET-Norway, NERSC, NILU, UiB, UiO, UNI	Norway	288×192 L32
TaiESM1	Research Center for Environmental Changes, Academia Sinica, Nankang(AS-RCEC)	Taiwan	288×192 L30

Table S 2: The similarity distance metric S_{ij} between model i and model j. Small values indicate high dependency or high similarity between two models.

	EC-Earth3	CanESM5	EC-Earth3-Veg	KACE-1-0-G	BCC-CSM2-MR	GFDL-ESM4	FGOALS-g3
ACCESS-CM2	0.70	0.66	0.68	0.68	0.79	0.80	0.80
ACCESS-ESM1-5	0.70	0.68	0.70	0.69	0.79	0.80	0.80
BCC-CSM2-MR	0.73	0.73	0.73	0.76	0.00	0.81	0.84
CanESM5	0.60	0.00	0.63	0.63	0.73	0.76	0.78
CESM2-WACCM	0.69	0.68	0.69	0.70	0.77	0.78	0.79
CESM2	0.67	0.71	0.71	0.71	0.79	0.78	0.82
CMCC-CM2-SR5	0.63	0.62	0.62	0.66	0.73	0.77	0.78
CMCC-ESM2	0.63	0.64	0.62	0.65	0.75	0.77	0.78
EC-Earth3-Veg-LR	0.61	0.64	0.61	0.69	0.74	0.77	0.79
EC-Earth3-Veg	0.55	0.63	0.00	0.67	0.73	0.74	0.73
EC-Earth3	0.00	0.60	0.55	0.65	0.73	0.75	0.76
FGOALS-g3	0.76	0.78	0.73	0.80	0.84	0.83	0.00
GFDL-ESM4	0.75	0.76	0.74	0.77	0.81	0.00	0.83
INM-CM4-8	0.73	0.70	0.71	0.72	0.82	0.83	0.84
INM-CM5-0	0.73	0.72	0.72	0.76	0.83	0.85	0.82
IPSL-CM6A-LR	0.63	0.63	0.62	0.66	0.74	0.75	0.78
KACE-1-0-G	0.65	0.63	0.67	0.00	0.76	0.77	0.80
MIROC6	0.68	0.71	0.71	0.74	0.79	0.80	0.81
MPI-ESM1-2-HR	0.74	0.72	0.73	0.76	0.80	0.82	0.84
MPI-ESM1-2-LR	0.71	0.71	0.74	0.72	0.77	0.79	0.82
MRI-ESM2-0	0.68	0.71	0.72	0.73	0.80	0.81	0.83
NorESM2-LM	0.71	0.70	0.70	0.74	0.76	0.80	0.82
NorESM2-MM	0.70	0.71	0.71	0.74	0.80	0.81	0.82
TaiESM1	0.65	0.65	0.67	0.68	0.75	0.77	0.81
Sum	15.65	15.69	15.70	16.33	17.82	18.15	18.50

Table S 3: Statistics of 20 year and 50 year return levels of the annual largest daily rainfall (unit: mm) averaged over 47 grids in Iran for the observations (OBS) and the future periods; P1 (2021-2050), P2 (2046-2075), and P3 (2071-2100) under the SSP2, SSP3, and SSP5 scenarios.

			SSP2-4.5			SSP3-7.0			SSP5-8.5		
Year	Statistic	OBS	P1	P2	P3	P1	P2	P3	P1	P2	P3
20-year	Mean	54	60	61	62	60	62	66	60	64	69
	Q1	46	51	51	52	49	51	54	51	55	59
	Median	57	64	64	65	63	65	71	64	69	73
	Q3	63	71	72	74	71	73	79	71	75	79
50-year	Mean	66	73	75	76	74	77	82	74	79	86
	Q1	57	63	65	65	62	64	69	65	70	77
	Median	71	78	82	83	80	81	86	79	84	89
	Q3	77	85	87	89	87	90	97	85	91	99

Table S 4: Relative change (unit: %) in 20 year and 50 year return levels of the annual largest daily rainfall averaged over Iran from 1971 to 2014.

		SSP2-4.5			SSP3-7.0			SSP5-8.5		
		P1	P2	P3	P1	P2	P3	P1	P2	P3
20-year	Mean	10.9	13.4	14.9	10.9	14.8	23.1	12.3	19.4	28.7
	Q1	7.5	10.2	12.6	7.6	11.9	18.7	9.7	15.7	24.6
	Median	11.9	13.9	15.6	11.2	14.7	23.2	12.3	19.6	28.7
	Q3	14.2	17.0	18.2	14.2	18.0	27.1	16.0	23.2	32.1
50-year	Mean	11.4	13.7	15.8	12.1	15.8	24.4	12.8	20.4	30.3
	Q1	7.1	10.9	12.9	8.5	11.8	19.7	8.7	15.6	24.7
	Median	12.9	13.6	17.5	11.6	15.7	25.2	13.9	20.4	30.0
	Q3	15.1	18.3	19.6	15.8	19.2	28.7	17.9	25.3	35.0

Table S 5: Spatially averaged exceedance probabilities over Iran for the annual maximum daily precipitation (AMP1) from 20 mm to 100 mm, obtained from the observations (OBS) and the CMIP6 models under the three scenarios for three future periods.

	AMP1	OBS	SSP2-4.5	SSP3-7.0	SSP5-8.5
Period 1	20mm	0.736	0.790	0.756	0.806
	30mm	0.334	0.368	0.357	0.454
	40mm	0.114	0.160	0.153	0.160
	50mm	0.030	0.070	0.075	0.077
	60mm	0.010	0.028	0.025	0.030
	80mm	0.001	0.004	0.004	0.008
	100mm	<0.001	0.001	0.001	0.002
Period 2	20mm	0.736	0.832	0.798	0.827
	30mm	0.334	0.424	0.380	0.435
	40mm	0.114	0.186	0.174	0.200
	50mm	0.030	0.078	0.073	0.092
	60mm	0.010	0.027	0.031	0.041
	80mm	0.001	0.005	0.004	0.011
	100mm	<0.001	0.002	0.001	0.004
Period 3	20mm	0.736	0.802	0.823	0.851
	30mm	0.334	0.394	0.469	0.470
	40mm	0.114	0.161	0.213	0.245
	50mm	0.030	0.064	0.098	0.126
	60mm	0.010	0.023	0.038	0.050
	80mm	0.001	0.005	0.007	0.013
	100mm	<0.001	0.002	0.003	0.004

Table S 6: The expected frequency of reoccurring years during 30 years for specific the annual maximum daily precipitation (AMP1) values from 20 mm to 100 mm in Iran, obtained from the observations (OBS) and the CMIP6 models under the 3 scenarios for 3 future periods.

		SSP2-4.5			SSP3-7.0			SSP5-8.5		
AMP1	OBS	P1	P2	P3	P1	P2	P3	P1	P2	P3
20mm	22.080	23.700	24.960	24.060	22.680	23.940	24.690	24.180	24.810	25.530
30mm	10.020	11.040	12.720	11.820	10.710	11.400	14.070	13.620	13.050	14.100
40mm	3.420	4.800	5.580	4.830	4.590	5.220	6.390	4.800	6.000	7.350
50mm	0.900	2.100	2.340	1.920	2.250	2.190	2.940	2.310	2.760	3.780
60mm	0.300	0.840	0.810	0.690	0.750	0.930	1.140	0.900	1.230	1.500
80mm	0.030	0.120	0.150	0.150	0.120	0.120	0.210	0.240	0.330	0.390
100mm	0.012	0.030	0.060	0.060	0.030	0.030	0.090	0.060	0.120	0.120

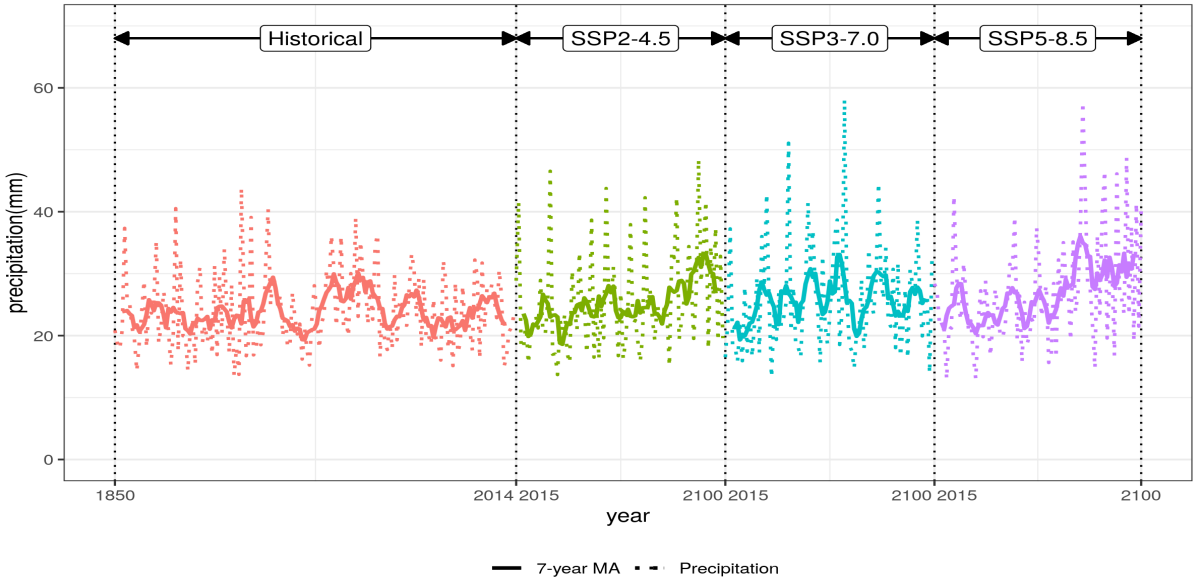

Figure S 3: Arrangement of data and 7 year moving averages composed of the historical data from 1850 to 2014 and the future data from 2015 to 2100 under SSP2, SSP3, and SSP5 scenarios for computing the Spearman correlation coefficient between models.

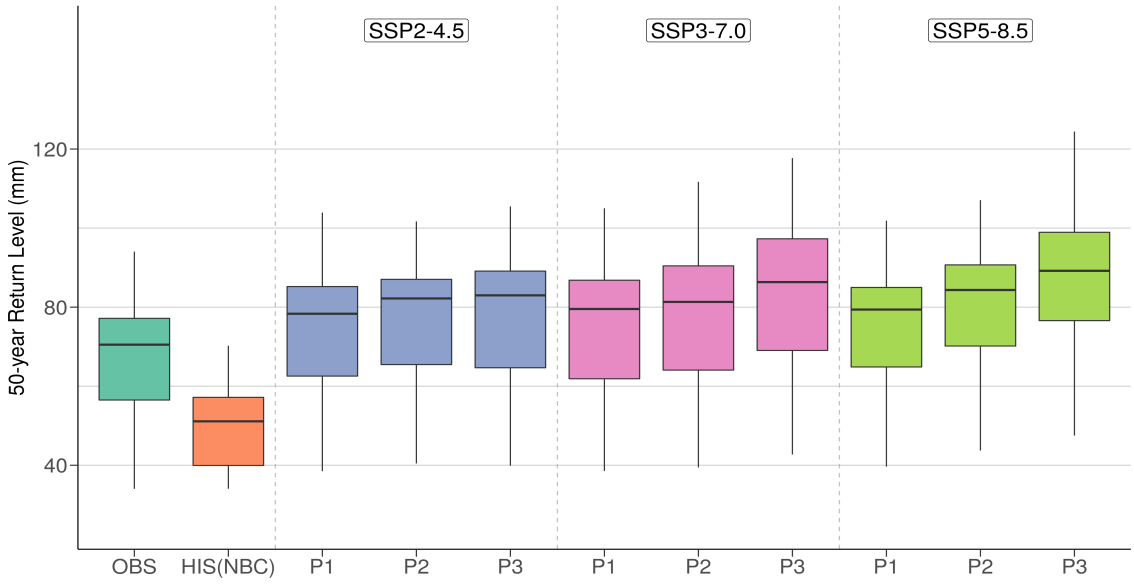

Figure S 4: Box-plots of 50 year return levels of the annual largest daily rainfall (unit: mm) averaged over 47 grids in Iran for the future periods P1 (2021–2050), P2 (2046–2075), and P3 (2071–2100) under the SSP2, SSP3, and SSP5 scenarios. OBS and HIST(NBC) stand for the observations and the historical data without bias correction.

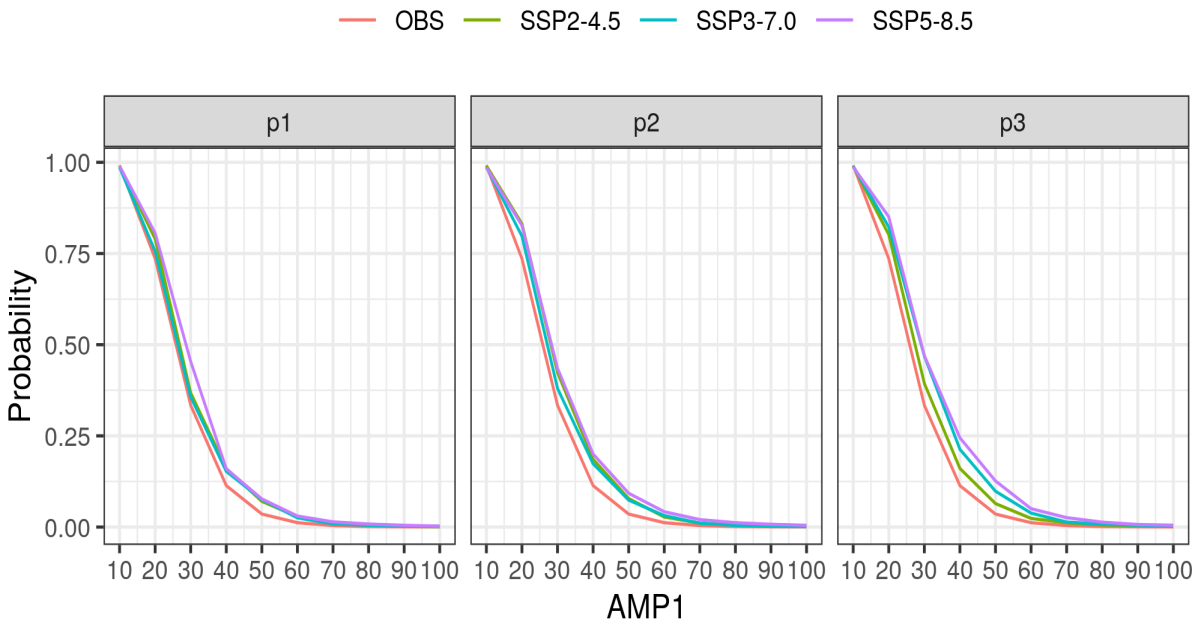

Figure S 5: The exceedance probability plots for the annual maximum daily precipitation (AMP1) from 10 mm to 100 mm in Iran, calculated from the observations (OBS) and the CMIP6 models under the three scenarios for three future periods.